High-Temperature Corrosion Behavior of Fe-18Ni-12Cr-2.9Al and Fe-18Ni-12Cr-2.3Al-Nb-C Austenitic Steels Depending on Dissolved Oxygen Concentration in Static Liquid Pb at 700 °C

Valentyn Tsisar[1,2] · Zhangjian Zhou[3] · Olaf Wedemeyer[1] · Aleksandr Skrypnik[1] · Jürgen Konys[1] · Carsten Schroer[1]

Abstract

The corrosion behavior of the aluminum-alloyed austenitic steels Fe-18Ni-12Cr-2.9Al and Fe-18Ni-12Cr-2.3Al-Nb-C was investigated at 700 °C in static Pb for 1000 h as a function of the concentration of dissolved oxygen in the liquid metal. In Pb with ~ 5×10^{-9} mass % dissolved oxygen, both steels showed dissolution. Depth of corrosion averaged 67 ($\pm$ 18) μm and 78 ($\pm$ 25) μm for Fe-18Ni-12Cr-2.3Al-Nb-C and Fe-18Ni-12Cr-2.9Al, respectively. In Pb with higher oxidation potential of 2×10^{-6} mass %O, both steels showed protective and accelerated oxidation. The protective thin oxide film (≤ 1 μm) was composed of outermost Fe-rich, interme-diate Cr-rich and inner Al-rich sublayers. The thicker oxide scale was of irregular thickness ($2 \div 30$ μm) and consisted of Fe–Cr mixed oxide with Ni-rich metallic inclusions.

Keywords Lead · Steel · Corrosion · Oxidation · Dissolution

Introduction

The corrosion resistance of steels against lead-based melts (Pb, Pb–Bi eutectic) is an important issue that may limit the temperature range of application of these func-tional media in next generation nuclear reactor systems (Gen IV and ADS) [1–3] or other application in the field of high-temperature energy conversion [4, 5]. It is well known that in order to improve the performance of austenitic and ferritic/martensitic steels in the presence of lead melts, it is necessary to ensure preferential in situ oxi-dation, thus avoiding the undesirable and more corrosive dissolution (leaching) of steel constituents such as Ni, Mn, Cr and Fe [6]. Therefore, the oxidation potential

of the liquid metal should be kept at a sufficiently high level, i.e., higher than necessary for the thermodynamic stability of the Fe oxide magnetite ($\sim 10^{-7} \div 10^{-6}$ mass% in the temperature range ~ 350–600 °C). When the oxygen concentration in the molten metal is maintained at this level, the oxidation of steels shows three main stages. It begins with the formation of a thin, rather Cr-rich oxide film. In the second stage, localized enhanced oxidation results in Fe-rich magnetite nodules, evolving, in the ideal case, into continuous bilayer Fe_3O_4/$(Fe,Cr)_3O_4$ oxide scale that grows with time according to a parabolic rate law (third stage). The latter is considered as an accelerated oxidation, which leads to a significant regression of the steel substrate, with the inner $(Fe,Cr)_3O_4$ spinel clearly growing into the steel matrix. The main issue for the bilayer Fe-based scales is their long-term durability. When the bilayer scale degrades and liquid metal contacts the unprotected steel surface, corrosion occurs by leaching of steel constituents (dissolution) even though the oxidation potential of the liquid metal bulk is high [7].

Improving the oxidation resistance of steels in lead melts is a challenging task. Based on the experience from oxidation in gases, it is natural to propose the application of more thermodynamically stable oxide films with lower mobility of ions than in the Fe-based oxide scale, especially for mastering molten lead at temperatures > 600 °C [6]. Therefore, so-called Alumina-Forming Austenitic (AFA) stainless steels with improved creep and oxidation resistance at high temperatures in gaseous media are of great interest for use in lead melts. The main attraction of AFA steels lies in the formation of a thin and protective alumina (Al_2O_3) film, in contrast to the conventional austenitic steels that produce considerably thicker, multilayer Fe-based scales as described above. However, the prerequisites for the formation of continuous Al_2O_3 in liquid lead, especially the minimum of dissolved oxygen that must be available, still need to be defined or confirmed.

Experiments carried out at temperatures ≤ 550 °C show that, similar to conventional austenitic steels not alloyed with Al, the concentration of dissolved oxygen in the liquid Pb and Pb-Bi eutectic should be higher than that required for the thermodynamic stability of magnetite (Fe_3O_4) in order to ensure in situ oxidation of the steel surface in the liquid metal [8, 9]. At 550 °C in static Pb with about 10^{-7} mass% dissolved oxygen Fe-14Cr-14Ni-2.5Al-1.6Mn-2.5Mo-0.9Nb steel forms a 100 nm thick protective Al-rich oxide film after one year of exposure allowing it to be characterized as a potential candidate material for use in Pb-cooled reactors [10].

In the case of high-Ni alloys, the Fe-(20-29)Ni-(15.2-16.5)Cr-(2.3-4.3)Al composition is proposed as optimal, based on the results of tests performed for 1000 h at 550 °C in stagnant Pb with 10^{-6} mass% O [11]. The protective oxide film formed was composed of Cr_2O_3 and Al_2O_3-Cr_2O_3 mixed oxide.

Thin oxide films formed on Fe-14Cr-2Mn-20Ni-0.5Cu-3Al and Fe-14Cr-5Mn-12Ni-3Cu-2.5Al steels (~ 200 nm thick bilayer Cr(Fe)-O/Al-O and ~ 50 nm thick single layer Al(Mn, Fe, Cr)-O, respectively) at 500 °C in static Pb-Bi eutectic show durability when changing the corrosion conditions in the liquid metal repeatedly from oxidizing to dissolving [12].

There is a significant gap in the corrosion testing of AFA steels under flowing conditions. Shen and co-authors report excellent corrosion resistance of Fe-14Ni-14Cr-2.5Al steel for 4008 h exposure to flowing (1.8 m/s) Pb-Bi eutectic with 5×10^{-7}—5×10^{-6}

mass% dissolved oxygen at 550 °C [13], which suggests formation of a thin and protective Al_2O_3 scale.

High-temperature tests (≥ 550 °C) of Al-alloyed austenitic steels in Pb-based melts are also still scarce. Recently, Pint et al. carried out tests at 600–800 °C, in both static and flowing Pb, on AFA steels [14]. During the static test at 600 °C, the AFA steels show better corrosion behavior than conventional 316H steel because of the formation of an Al-rich oxide film. However, at higher testing temperature of 700 or 800 °C, AFA steels exhibit greater mass loss related to dissolution in comparison with 316H steel. In 0.8 m/s flowing Pb at 650 °C, circulated in a loop made of Fe–Cr-Al steel, dissolution of the AFA steels is < 10 μm after 1000 h of exposure. It is important to note that oxygen control was not implemented at this stage of loop operation.

The objective of this study is to improve the understanding of the high-temperature corrosion performance of Al-alloyed austenitic steels by testing at 700 °C in stagnant Pb, taking into account the concentration of oxygen dissolved in the liquid metal.

Experimental Procedures

Materials

Cylindrical specimens (Ø8 × 10 mm) made of Fe-18Ni-12Cr-2.9Al and Fe-18Ni-12Cr-2.3Al-Nb-C austenitic steels were used for corrosion test. Samples were manufactured by means of electrical discharge machining (EDM) followed by the fine turning of surface as a final step in samples preparation. Then, samples were cleaned ultrasonically in acetone and ethanol.

Table 1 shows detailed composition of the steels verified by means of inductively coupled plasma optical emission spectroscopy (ICP-OES) and energy-dispersive X-ray (EDX) analysis. For element determination using ICP-OES, the sample was dissolved with acid in an ultrasonic bath. Carbon was analyzed using a Carbon/Sulfur (CS) analyzer.

Figure 1 visualizes the microstructure of steels as the image quality (IQ) maps constructed from electron backscatter diffraction (EBSD) data. The average grain size of Fe-18Ni-12Cr-2.9Al is 35 μm, which is approximately twice the grain size of the 18 μm in the more complex alloyed Fe-18Ni-12Cr-2.3Al-Nb-C steel. The latter steel is strengthened by Nb(Ti) carbides and Laves phases which are the grain boundary pinning agents preventing grain growth during heat treatment and aging. The detailed information about composition and structure of tested steels one could find elsewhere [15, 16].

Testing Method

Figure 2 presents the experimental apparatus design used to conduct static corrosion tests in liquid metals. The apparatus comprises an alumina crucible filled with 2 kg of lead, which is placed inside a steel capsule. The top of the capsule features a lid housing multiple work ports, including those for gas inlet and outlet, thermocouples

Table 1 Average chemical composition (mass%) of the aluminum-alloyed austenitic steels according to different methods of analysis

Element	Fe-18Ni-12Cr-Al		Fe-18Ni-12Cr-Al-Nb-C	
	ICP-OES	EDX	ICP-OES	EDX
	Mean (Standard Deviation)	Mean	Mean (Standard Deviation)	Mean
C*	0.0300 (0.0006)		0.0086 (0.0003)	
Al	2.90 (0.010)	2.71	2.32 (0.008)	2.12
Si	0.377 (0.0009)		0.401 (0.0006)	
Ti	0.0234 (0.0006)		0.0568 (0.0003)	
V	0.0038 (0.0001)		0.0048 (0.0001)	
Cr	11.7 (0.03)	12.30	11.7 (0.02)	12.55
Mn	0.118 (0.0005)		0.0887 (0.0003)	
Fe	64.3 (0.30)	Bal	64.4 (0.08)	Bal
Ni	18.0 (0.05)	16.58	18.0 (0.02)	16.89
Cu	0.0081 (0.0006)		0.0031 (0.0001)	
Nb	<0.001		0.577 (0.003)	
Mo	2.00 (0.007)		1.99 (0.003)	
W	0.0010 (0.0001)		0.0031 (0.0005)	

*concentration of carbon was measured by CS analyzer
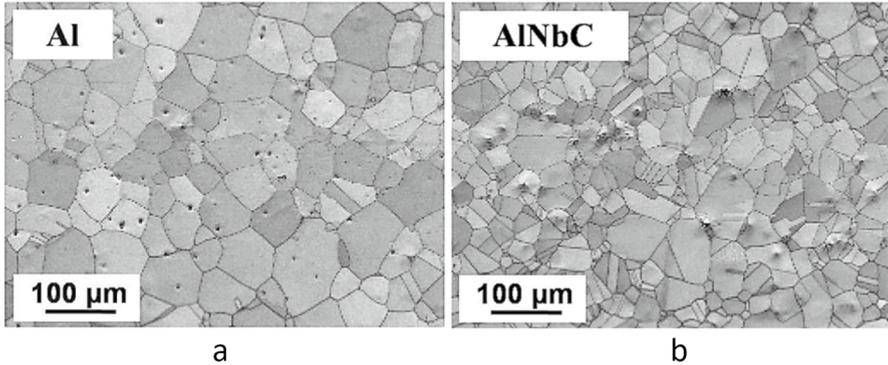
Fig. 1 Microstructure of **a** Fe-18Ni-12Cr-2.9Al (**Al**) and **b** Fe-18Ni-12Cr-2.3Al-Nb-C (**AlNbC**) austenitic steels

safeguarded by alumina tubes, an electrode that closes an electric circuit, a specimen rod holder made of Mo, and two electrochemical oxygen sensors positioned in the middle and at the top of the liquid bath. The capsule is placed in the vertical furnace.

Before performing the corrosion test, the liquid metal is pre-conditioned to achieve the desired oxygen concentration using the oxygen control system (OCS) developed by the Karlsruhe Institute of Technology (KIT). The OCS enables active monitoring and control of oxygen concentration in the liquid Pb and Pb-Bi eutectic.
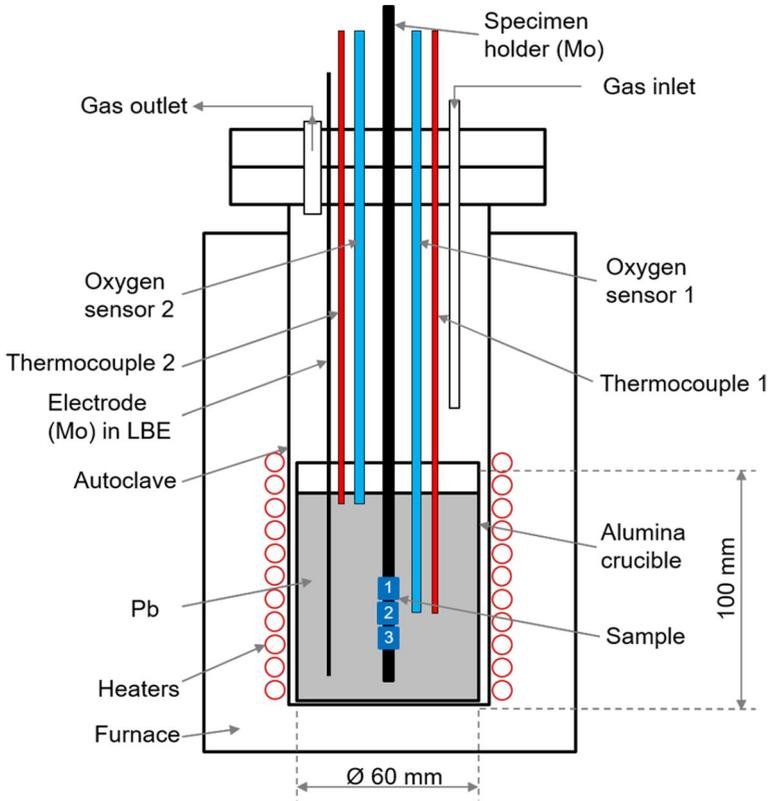
Fig. 2 Principal scheme of apparatus for corrosion tests in liquid metals

The working gases, including Ar, Ar-5vo 1%H$_2$, and synthetic air, flow across the surface of the liquid metal. Electrochemical oxygen sensors with a Pt/air reference electrode were utilized to monitor and regulate the concentration of oxygen in the liquid lead. The sensor output was converted into the oxygen concentration in Pb by using the following formula [17]:

$$\log C_O(\text{mass}\%) = -2.3335 + \frac{6338.1}{T(K)} - 10080\frac{E(V)}{T(K)} \tag{1}$$

When the output of Sensor 1 (S1), positioned at the sample level, reaches a stable target value, the sample holder is submerged into the liquid metal through the tube port (Fig. 2).

Two corrosion tests were carried at 700 °C in stagnant liquid Pb for 1000 h, depending on the oxygen concentration in the liquid metal. The first test was carried out in Pb with controlled oxygen concentration of ~2×10^{-6} mass %, which, based on thermodynamic evaluations, was expected to result in oxidation of steels [17]. The second test was performed in liquid Pb with "low" oxygen concentration of ~5×10^{-9} mass % dissolved oxygen, which was expected to lead to the domination

of the dissolution corrosion mode. For each test condition, one sample (Ø8×10 mm) of each steel is used.

After the corrosion tests were completed, the samples were segmented through cutting, and metallographic cross sections were prepared. To determine the corrosion losses, the metallographic method was used by comparing the initial diameter ($\text{Ø}_{in.}$) of the samples with the post-test diameter ($\text{Ø}_{cor.}$) of samples not affected by corrosion. Twelve measurements were taken at 15-degree intervals along the guide lines to obtain a set of regular corrosion depths (Fig. 3). Furthermore, a metallographic examination was used to measure the maximum corrosion depth along the circumference of the cross section. The obtained results were statistically elaborated and the corrosion data are presented as the average value of corrosion depth with maximum and minimum deviations. The percentage of corrosion coverage (dissolution or oxidation) was determined by observing 24 regularly spaced cross sections near a guide line that crosses the interface between the steel surface and the solidified Pb (%=(i×100)/24, where i – corrosion appearance, i.e., protective oxidation; accelerated oxidation; dissolution).

The evaluation of the morphologies and compositions of corrosion zones was carried out using a scanning electron microscope (SEM) equipped with an energy-dispersive X-ray spectrometer (EDX). The composition of thin oxide films was determined through Auger electron spectroscopy using the PHI 680 Xi Auger nanoprobe.

Fig. 3 a Methodology of measuring of corrosion depth and diameter change ($\text{Ø}_{in.}$ vs $\text{Ø}_{cor.}$) along the circumference of cross section **b** obtained by light optical microscopy
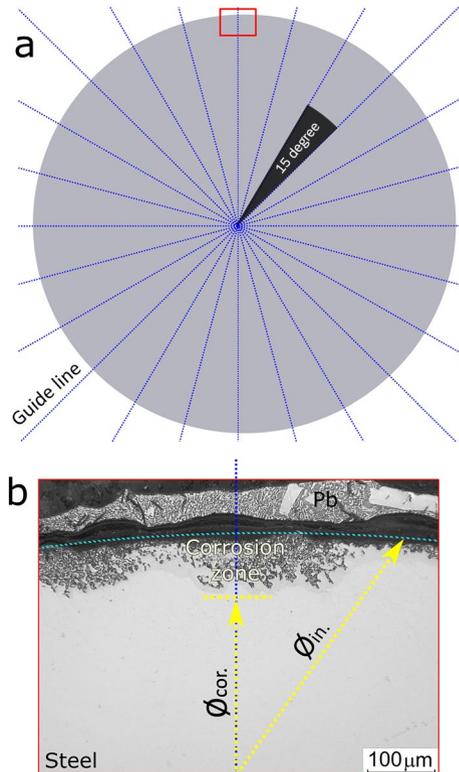
Results and Discussion

Figure 4 displays the correlation between the corrosion depth, measured on the metallographic cross section of steels, and the concentration of dissolved oxygen in liquid lead at 700 °C for 1000 h. The corrosion depth decreases significantly as the concentration of dissolved oxygen in the liquid lead increases from approximately 5×10^{-9} to about 2×10^{-6} mass%. Furthermore, the steel's corrosion modes vary with the predominance of dissolution and oxidation, respectively. The obtained results are aligned with thermodynamic considerations [17] and are in agreement with commonly accepted concepts on corrosion interaction in the solid steel/liquid lead system [3].

### Pb with ~ 2 × 10⁻⁶ Mass% Dissolved Oxygen—Oxidation Regime

In the presence of liquid lead containing $\sim 2 \times 10^{-6}$ mass% dissolved oxygen, both steels were found to undergo protective and accelerated oxidation (Fig. 5, 6, 7, 8). Corrosion depth measured on cross sections as the change between the initial ($\emptyset_{in.}$) and post-test ($\emptyset_{cor.}$) diameters of the specimens (Fig. 3) averages approximately 2 μm for both steels (Fig. 4 oxidation region).

The Fe-18Ni-12Cr-2.3Al-Nb-C steel demonstrates protective oxidation on 96% of its sample surface. Localized accelerated oxidation was observed on the remaining 4% of the surface, with an average measurable thickness of 3.9 (± 4.2) μm and a maximum thickness of 13.7 μm.

The Fe-18Ni-12Cr-2.9Al alloy showed protective oxidation on 75% of the surface area, with the remaining 25% demonstrating accelerated oxidation. The developed oxide scales were thicker compared to the more complex alloyed steel, with an average thickness of 9.8 (± 5.4) μm and a maximum thickness of 31 μm.

Protective oxidation results in the formation of a thin (≤ 1 μm) aluminum-enriched oxide film, as shown in Fig. 5c. Auger electron spectroscopy analysis

Fig. 4 Corrosion depth measured on Fe-18Ni-12Cr-2.9Al and Fe-18Ni-12Cr-2.3Al-Nb-C austenitic steels after corrosion tests at 700 °C for 1000 h depending on the concentration of oxygen dissolved in liquid Pb. Vertical short dash dot line shows theoretical concentration of oxygen in liquid lead which correspond to the thermodynamic equilibrium between Fe/Fe$_3$O$_4$
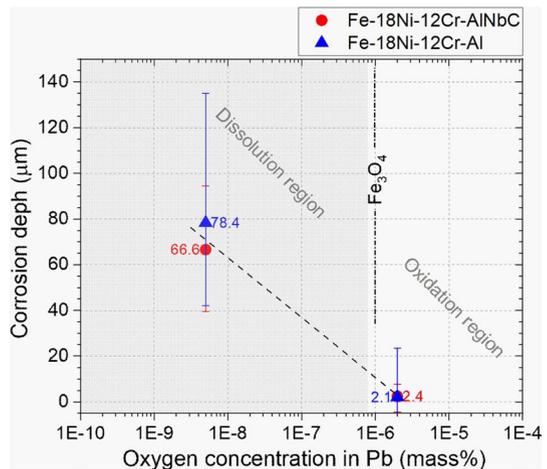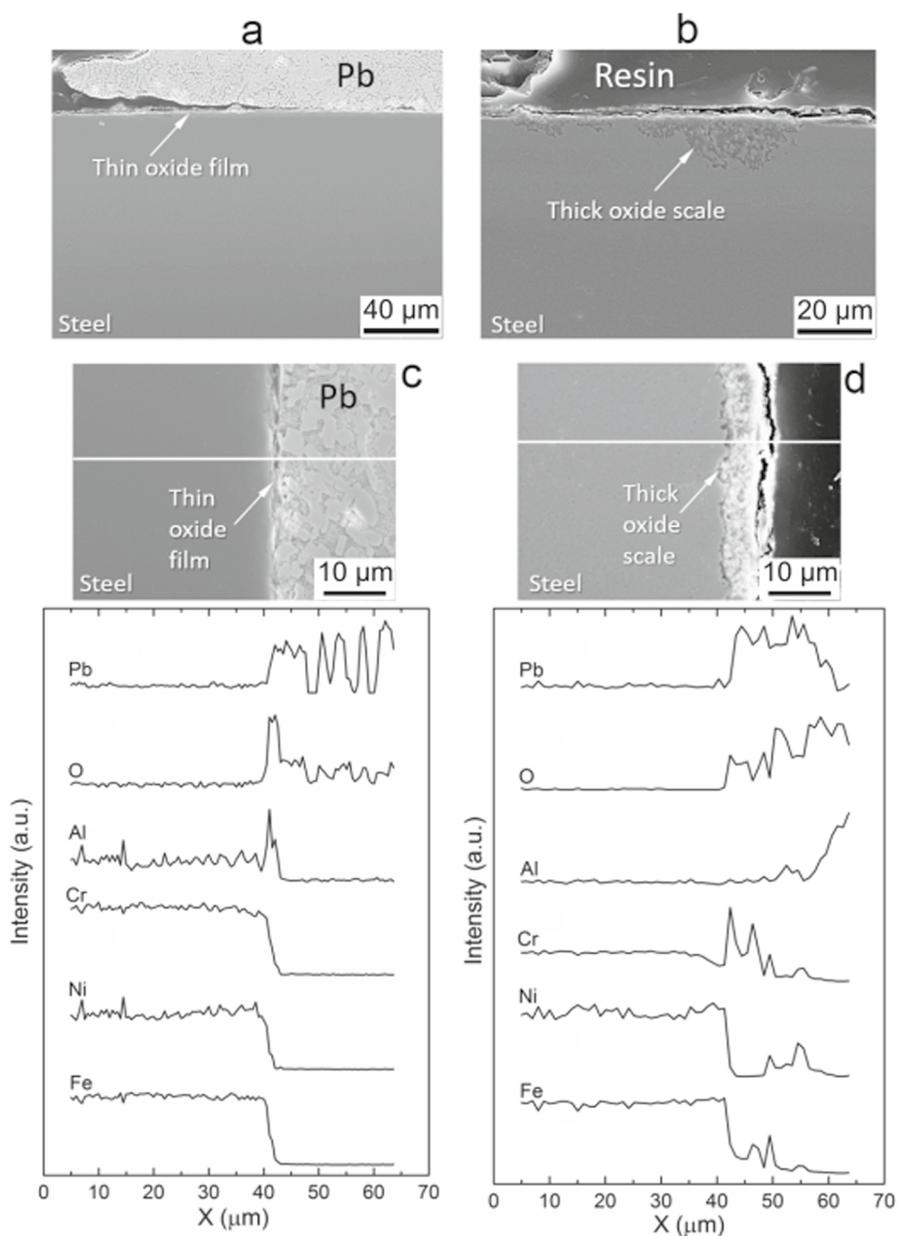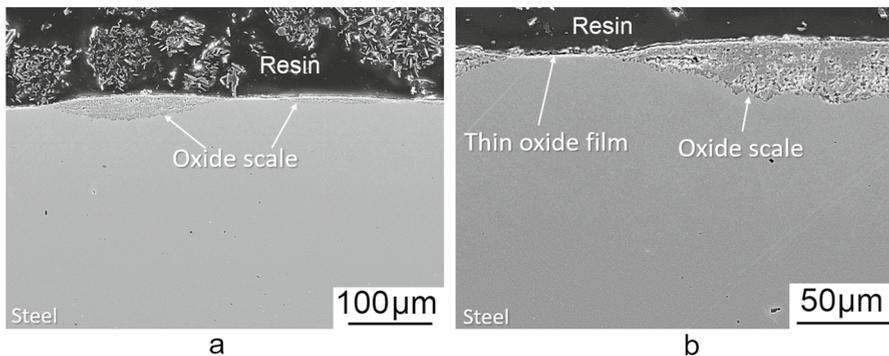
Fig. 5 Oxidation behavior of Fe-18Ni-12Cr-2.3Al-Nb-C austenitic steels at 700 °C in static liquid Pb with 2×10^{-6} mass % O for 1000 h. a and c show formation of thin Al-rich oxide film (EDX profile) observed on the 96% of sample surface. b and d show localized accelerated oxidation observed on the 4% of sample surface in the view of Fe–Cr mixed oxide (EDX profile)
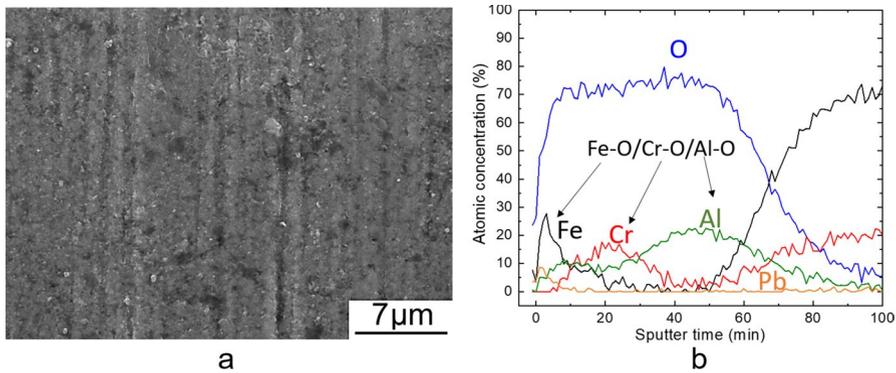
Fig. 6 **a** Surface morphology and **b** corresponding Auger sputter depth profile from the surface of Fe-18Ni-12Cr-2.3Al-Nb-C steel sample after the test at 700 °C in static liquid Pb with 2×10^{-6} mass % O for 1000 h


Fig. 7 **a** General and **b** detailed cross section views of oxidation behavior of Fe-18Ni-12Cr-2.9Al austenitic steels at 700 °C in static liquid Pb with 2×10^{-6} mass % O for 1000 h. Localized accelerated oxidation observed on the 25% of sample surface in the view of Fe–Cr mixed oxide

of Fe-18Ni-12Cr-2.3Al-Nb-C steel sample surface, as presented in Fig. 6a, reveal more complex-layered structure of the oxide film with outer Fe-rich, intermediate Cr-rich, and inner Al-rich sub-oxide layers of varying aluminum content (Fig. 6b).

The accelerated oxidation results in the formation of thicker porous oxide scales that are enriched with chromium, as shown in Figs. 5b, d, 7, and 8. Nickel does not play a role in the oxidation process and appears in the oxide scale as regions enriched with nickel (Fig. 8). The oxide scales remain impervious to Pb penetration during the given test duration.

The oxidation of conventional steels (not alloyed by Al) in liquid Pb or Pb-Bi eutectic is controlled by outward diffusion of Fe-cations which, in the ideal case, results in formation of bilayer scale consisting of outer Fe_3O_4 (magnetite) and inner chromium deficient spinel $Fe_{3-x}Cr_xO_4$ followed by the internal oxidation zone (IOZ)

Fig. 8 Morphology and elemental EDX profile along the oxide scale formed on the surface of Fe-18Ni-12Cr-2.9Al austenitic steels at 700 °C in static liquid Pb with 2×10^{-6} mass %O for 1000 h
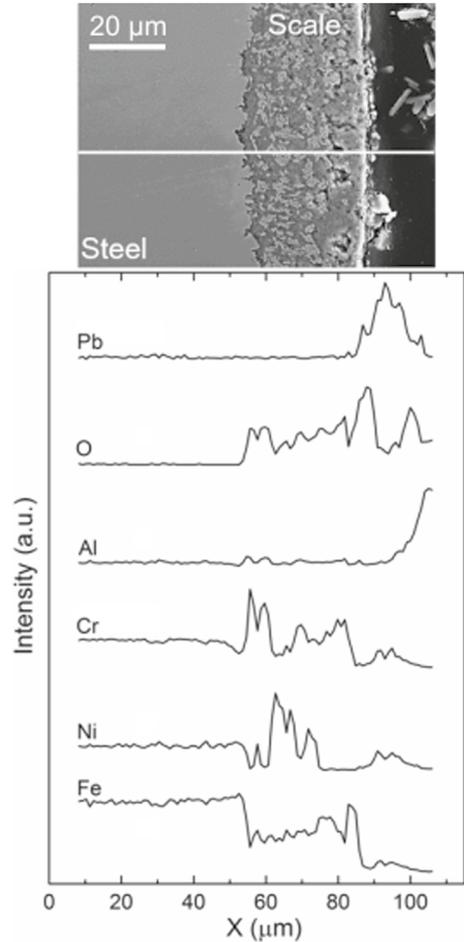
[7, 18–21]. In this work, the protective thin oxide film and non-protective thick scale are formed on the surface of both steels. The thin oxide film consists of the outer Fe-rich, intermediate Cr-rich and inner Al-rich oxide sub-layers, while the thicker scale could be represented as a $Fe_{3-x}Cr_xO_4$ spinel with inclusions of metallic Ni. In both cases, the oxidation is controlled by outward diffusion of Fe cations, which, however, is substantially slower in the case of protective oxidation since the inner Cr- and Al-rich sub-layers are better barrier with respect to outward diffusion of Fe-cations [22]. The accelerated oxidation is a result of the breakaway oxidation of initially formed protective oxide film [23]. The better oxidation behavior of Fe-18Ni-12Cr-2.3Al-Nb-C steel compared to Fe-18Ni-12Cr-2.9Al could be explained by more fine-grained structure and presence of B2-NiAl precipitates in the composition of more complex alloyed steel [15]. Both mentioned structural features favor easier origination and diffusion of alloying elements into oxide film, while the precipitates

are the additional source of Al for the formation and growth of protective Al-rich oxide film.

Pb with ~ 5 × 10⁻⁹ Mass% Dissolved Oxygen—Dissolution Regime

In lead with ~ 5×10^{-9} mass% dissolved oxygen, both steels underwent noticeable dissolution. The latter resulted in the formation of a corrosion zone infiltrated by lead and significantly depleted in nickel and chromium in comparison with the bulk composition of steels, as shown in Fig. 9. Corrosion coverage on the surface of both steels was 100%. The depth of corrosion zone was found to be 67 (±18) μm and 78 (±25) μm for Fe-18Ni-12Cr-2.3Al-Nb-C and Fe-18Ni-12Cr-2.9Al steels, respectively (Fig. 4 dissolution region). The maximum corrosion depth of Fe-18Ni-12Cr-2.3Al-Nb-C steel is 95 μm, whereas that of Fe-18Ni-12Cr-2.9Al steels reaches 135 μm.

Conclusions

The high-temperature corrosion behavior of aluminum-alloyed Fe-18Ni-12Cr-2.9Al and Fe-18Ni-12Cr-2.3Al-Nb-C austenitic steels in stagnant liquid Pb at 700 °C for ~ 1000 h was investigated. The effect of oxygen concentration dissolved in liquid metal is determined. Similar to the conventional austenitic steels, which are not alloyed with the aluminum, the oxidation potential of liquid Pb at 700 °C needs to be higher than necessary for the thermodynamic stability of magnetite ($\geq 10^{-6}$ mass%O) to ensure *in situ* oxidation of aluminum-alloyed austenitic steels:

1. In liquid Pb with ~ 5×10^{-9} mass % dissolved oxygen, both steels underwent the dissolution corrosion:

   - The dissolution resulted in formation of corrosion zone depleted in Ni and Cr and penetrated by Pb;
   - The average depth of corrosion attack was 67 (±18) μm and 78 (±25) μm for Fe-18Ni-12Cr-2.3Al-Nb-C and Fe-18Ni-12Cr-2.9Al steels, respectively;

2. Increase in oxygen concentration to about ~ 2×10^{-6} mass % promotes oxidation of both steels. Oxidation develops in protective and accelerated manner. It appears that more complex alloyed steel Fe-18Ni-12Cr-2.3Al-Nb-C with two times smaller grain size shows better oxidation resistance than Fe-18Ni-12Cr-2.9Al steel:

   - Fe-18Ni-12Cr-2.3Al-Nb-C steel shows protective oxidation on 96% of surface. The protective oxidation is accompanied by the formation of thin oxide film composed of outer Fe-rich, intermediate Cr-rich, and inner Al-rich sub-oxide layers. The remaining 4% of the surface exhibited accelerated oxidation, resulting in the formation of a Fe–Cr mixed oxide with Ni-rich metallic inclusions. Thickness of oxide ranges from 1 to 13.7 μm;
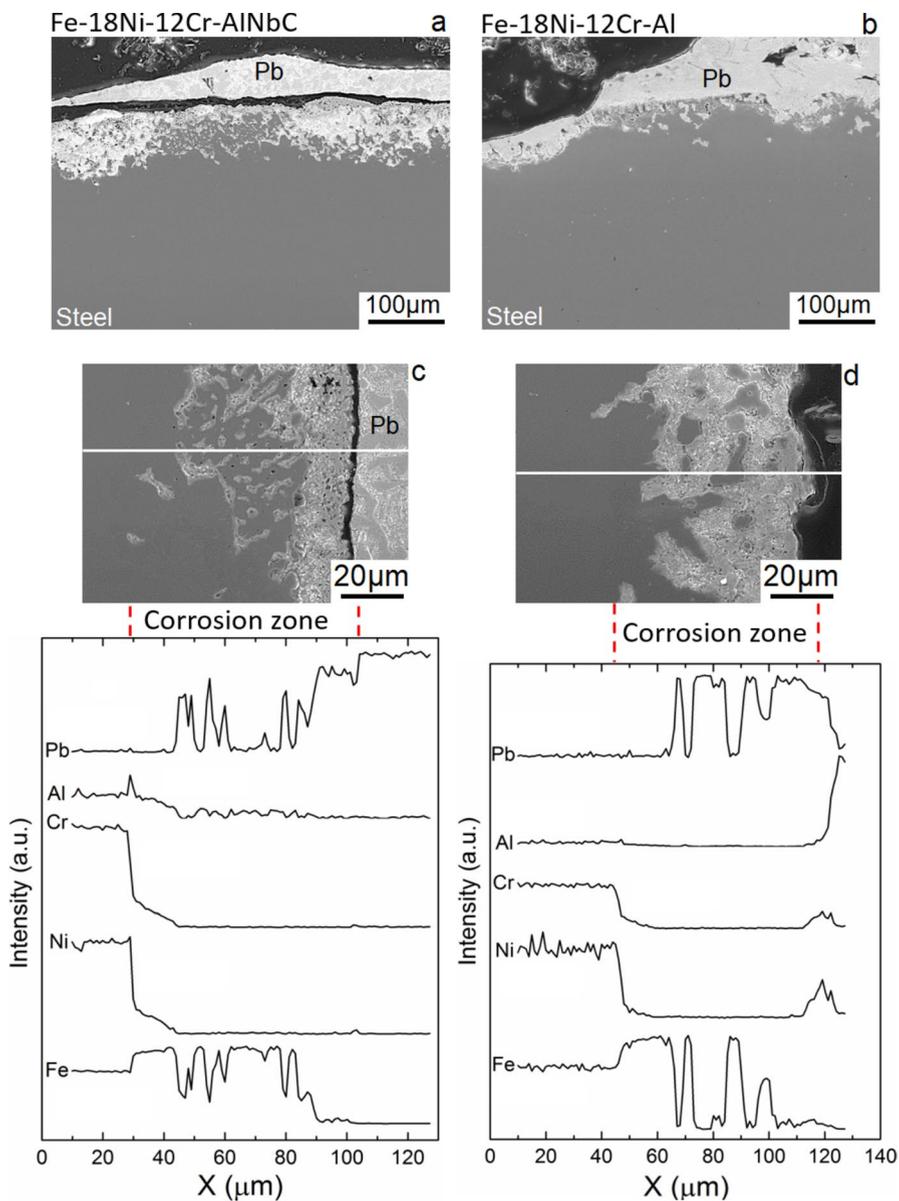
Fig. 9 Morphology and corresponding elemental profile along the corrosion zones formed on **a** and **c** Fe-18Ni-12Cr-2.3Al-Nb-C and **b** and **d** 18Ni-12Cr-2.9Al austenitic steels exposed at 700 °C to static liquid Pb with 5×10^{-9} mass %O for 1000 h

- Fe-18Ni-12Cr-2.9Al steel shows protective oxidation on 75% of the surface, while the remaining 25% demonstrates accelerated oxidation accompanied by formation of Fe–Cr mixed oxide with Ni-rich metallic inclusions. Thickness of oxide ranges from 3 to 31 μm.

Author's contribution VT wrote the main manuscript and prepared figures and table; CS reviewed the manuscript; ZZ provided material for the test and its description; OW provided technical support; AS provided technical support; and JK contributed to funding support and supervision.

Data availability No datasets were generated or analyzed during the current study.

Declarations

Conflict of interest The authors declare no competing interests.

References

1. OECD-NEA, *Handbook on lead-bismuth eutectic alloy and lead properties, materials compatibility, thermal-hydraulics and technologies,* (2015).
2. J. Zhang, *Liquid Metal Corrosion: Fundamental Theory and Applications*, (Woodhead Publishing, an imprint of Elsevier, Cambridge, MA, 2023).
3. F. Balbaud-Célérier, J.-L. Courouau, D. Féron, L. Martinelli, and F. Rouillard, in *Nuclear Corrosion: Research, Progress and Challenges*, Ritter S., ed., (Woodhead Publishing, 2020), p. 437.
4. J. Pacio and T. Wetzel, *Solar Energy* **93**, 2013 (11).
5. F. Müller-Trefzer, K. Niedermeier, M. Daubner, and T. Wetzel, *Applied Thermal Engineering* **213**, 2022 118619.
6. B. A. Shmatko and A. E. Rusanov, *Materials Science* **36**, 2000 (689).
7. V. Tsisar, C. Schroer, O. Wedemeyer, A. Skrypnik, and J. Konys, *Journal of Nuclear Materials* **494**, 2017 (422).
8. Valentyn Tsisar, Zhang Jian Zhou, Olaf Wedemeyer, Aleksandr Skrypnik, and Carsten Schroer, *Materials Science Forum* **1024**, 2021 (79).
9. M. Roy, L. Martinelli, K. Ginestar, J. Favergeon, and G. Moulin, *Journal of Nuclear Materials* **468**, 2016 (153).
10. J. Ejenstam and P. Szakálos, *Journal of Nuclear Materials* **461**, 2015 (164).
11. H. Shi, A. Jianu, A. Weisenburger, C. Tang, A. Heinzel, R. Fetzer, F. Lang, R. Stieglitz, and G. Müller, *Journal of Nuclear Materials* **524**, 2019 (177).
12. V. Tsisar, E. Stergar, S. Gavrilov, W. van Renterghem, P. Louette, and S. Lucas, *Corrosion Science* **195**, 2022 109963.
13. L. Shen, *Fe-14Ni-14Cr-2.5Al steel showing excellent corrosion-resistance in flowing LBE at 550 °C and high temperature strength*
14. B. A. Pint, Y.-F. Su, M. P. Brady, Y. Yamamoto, J. Jun, and M. R. Ickes, *JOM* **73**, (12), 2021 (4016).
15. M. Wang, H. Sun, M. P. Phaniraj, H. N. Han, J. Jang, and Z. Zhou, *Materials Science and Engineering: A* **672**, 2016 (23).
16. M. Wang, H. Sun, W. Zheng, and Z. Zhou, *Materials Today Communications* **25**, 2020 101303.
17. C. Schroer, O. Wedemeyer, and J. Konys, *Nuclear Engineering and Design* **241**, (12), 2011 (4913).
18. O. Yeliseyeva, V. Tsisar, and G. Benamati, *Corrosion Science* **50**, (6), 2008 (1672).
19. L. Martinelli, F. Balbaud-Célérier, A. Terlain, S. Delpech, G. Santarini, J. Favergeon, G. Moulin, M. Tabarant, and G. Picard, *Corrosion Science* **50**, 2008 (2523).

20. L. Martinelli, F. Balbaud-Célérier, G. Picard, and G. Santarini, *Corrosion Science* **50**, 2008 (2549).
21. L. Martinelli, F. Balbaud-Célérier, A. Terlain, S. Bosonnet, G. Picard, and G. Santarini, *Corrosion Science* **50**, 2008 (2537).
22. F. H. Stott, G. C. Wood, and J. Stringer, *Oxid Met* **44**, 1995 (113).
23. T. Gheno, D. Monceau, and D. Young, *Mechanism of Breakaway Oxidation of Fe–Cr and Fe–Cr–Ni Alloys in Dry and Wet Carbon Dioxide*

Authors and Affiliations

Valentyn Tsisar[1,2] · Zhangjian Zhou[3] · Olaf Wedemeyer[1] · Aleksandr Skrypnik[1] · Jürgen Konys[1] · Carsten Schroer[1]

✉ Valentyn Tsisar
valentyn.tsisar@sckcen.be

Zhangjian Zhou
zhouzhj@mater.ustb.edu.cn

Olaf Wedemeyer
olaf.wedemeyer@kit.edu

Aleksandr Skrypnik
aleksandr.skrypnik@kit.edu

Jürgen Konys
juergen.konys@t-online.de

Carsten Schroer
carsten.schroer@kit.edu

[1] Institute for Applied Materials–Applied Materials Physics (IAM-AWP), Karlsruhe Institute of Technology (KIT), Hermann-von-Helmholtz-Platz 1, 76344 Eggenstein-Leopoldshafen, Germany

[2] Nuclear Energy Technology, Structural Materials, Belgian Nuclear Research Centre SCK·CEN, Boeretang 200, 2400 Mol, Belgium

[3] School of Material Science and Engineering, University of Science and Technology Beijing, Beijing 100083, China